



HAL
open science

Myofibrillar misalignment correlated to triad disappearance of mdx mouse gastrocnemius muscle probed by SHG microscopy

Denis Rouède, Pascal Coumailleau, Emmanuel Schaub, Jean-Jacques Bellanger, Mireille Blanchard-Desce, François Tiaho

► To cite this version:

Denis Rouède, Pascal Coumailleau, Emmanuel Schaub, Jean-Jacques Bellanger, Mireille Blanchard-Desce, et al.. Myofibrillar misalignment correlated to triad disappearance of mdx mouse gastrocnemius muscle probed by SHG microscopy. *Biomedical optics express*, 2014, 5 (3), pp.858-875. 10.1364/BOE.5.000858 . hal-00952823

HAL Id: hal-00952823

<https://hal.science/hal-00952823v1>

Submitted on 27 Feb 2014

HAL is a multi-disciplinary open access archive for the deposit and dissemination of scientific research documents, whether they are published or not. The documents may come from teaching and research institutions in France or abroad, or from public or private research centers.

L'archive ouverte pluridisciplinaire **HAL**, est destinée au dépôt et à la diffusion de documents scientifiques de niveau recherche, publiés ou non, émanant des établissements d'enseignement et de recherche français ou étrangers, des laboratoires publics ou privés.

Myofibrillar misalignment correlated to triad disappearance of mdx mouse gastrocnemius muscle probed by SHG microscopy

Denis Rouède,¹ Pascal Coumailleau,² Emmanuel Schaub,¹ Jean-Jacques Bellanger,³ Mireille Blanchard-Desce,⁴ and François Tiaho^{2,*}

¹IPR, CNRS, UMR-CNRS URI- 6251, Université de Rennes1, Campus de Beaulieu, Rennes, F-35000, France

²IRSET, INSERM, U1085, Université de Rennes1, Campus de Beaulieu, Rennes, F-35000, France

³LTSI, INSERM, U1099, Université de Rennes1, Rennes, F-35000, France

⁴ISM, CNRS, UMR-CNRS 5255, Université de Bordeaux 1, Talence, F-33405, France

*francois.tiaho@univ-rennes1.fr

Abstract: We show that the canonical single frequency sarcomeric SHG intensity pattern (SHG-IP) of control muscles is converted to double frequency sarcomeric SHG-IP in preserved mdx mouse gastrocnemius muscles in the vicinity of necrotic fibers. These double frequency sarcomeric SHG-IPs are often spatially correlated to double frequency sarcomeric two-photon excitation fluorescence (TPEF) emitted from Z-line and I-bands and to one centered spot SHG angular intensity pattern (SHG-AIP) suggesting that these patterns are signature of myofibrillar misalignment. This latter is confirmed with transmission electron microscopy (TEM). Moreover, a good spatial correlation between SHG signature of myofibrillar misalignment and triad reduction is established. Theoretical simulation of sarcomeric SHG-IP is used to demonstrate the correlation between change of SHG-IP and -AIP and myofibrillar misalignment. The extreme sensitivity of SHG microscopy to reveal the submicrometric organization of A-band thick filaments is highlighted. This report is a first step toward future studies aimed at establishing live SHG signature of myofibrillar misalignment involving excitation contraction defects due to muscle damage and disease.

©2014 Optical Society of America

OCIS codes: (180.4315) Nonlinear microscopy; (190.4160) Multiharmonic generation; (170.3880) Medical and biological imaging.

References and links

1. K. P. Campbell and S. D. Kahl, "Association of dystrophin and an integral membrane glycoprotein," *Nature* **338**(6212), 259–262 (1989).
2. E. E. Zubrzycka-Gaarn, D. E. Bulman, G. Karpati, A. H. Burghes, B. Belfall, H. J. Klamut, J. Talbot, R. S. Hodges, P. N. Ray, and R. G. Worton, "The Duchenne muscular dystrophy gene product is localized in sarcolemma of human skeletal muscle," *Nature* **333**(6172), 466–469 (1988).
3. D. J. Blake, A. Weir, S. E. Newey, and K. E. Davies, "Function and genetics of dystrophin and dystrophin-related proteins in muscle," *Physiol. Rev.* **82**(2), 291–329 (2002).
4. J. G. Tidball and M. Wehling-Henricks, "The role of free radicals in the pathophysiology of muscular dystrophy," *J. Appl. Physiol.* **102**(4), 1677–1686 (2006).
5. G. Bulfield, W. G. Siller, P. A. Wight, and K. J. Moore, "X chromosome-linked muscular dystrophy (mdx) in the mouse," *Proc. Natl. Acad. Sci. U.S.A.* **81**(4), 1189–1192 (1984).
6. S. De la Porte, S. Morin, and J. Koenig, "Characteristics of skeletal muscle in mdx mutant mice," *Int. Rev. Cytol.* **191**, 99–148 (1999).
7. T. A. Partridge, "The mdx mouse model as a surrogate for Duchenne muscular dystrophy," *FEBS J.* **280**(17), 4177–4186 (2013).
8. B. Blaauw, L. Agatea, L. Toniolo, M. Canato, M. Quarta, K. A. Dyar, D. Danieli-Betto, R. Betto, S. Schiaffino, and C. Reggiani, "Eccentric contractions lead to myofibrillar dysfunction in muscular dystrophy," *J. Appl. Physiol.* **108**(1), 105–111 (2010).

9. A. Franco, Jr. and J. B. Lansman, "Calcium entry through stretch-inactivated ion channels in mdx myotubes," *Nature* **344**(6267), 670–673 (1990).
10. M. D. Teichmann, F. V. Wegner, R. H. Fink, J. S. Chamberlain, B. S. Launikonis, B. Martinac, and O. Friedrich, "Inhibitory control over Ca(2+) sparks via mechanosensitive channels is disrupted in dystrophin deficient muscle but restored by mini-dystrophin expression," *PLoS ONE* **3**(11), e3644 (2008).
11. P. R. Turner, T. Westwood, C. M. Regen, and R. A. Steinhardt, "Increased protein degradation results from elevated free calcium levels found in muscle from mdx mice," *Nature* **335**(6192), 735–738 (1988).
12. M. J. Cullen, J. J. Fulthorpe, and J. B. Harris, "The distribution of desmin and titin in normal and dystrophic human muscle," *Acta Neuropathol.* **83**(2), 158–169 (1992).
13. H. J. Binder, D. C. Herting, V. Hurst, S. C. Finch, and H. M. Spiro, "Tocopherol deficiency in man," *N. Engl. J. Med.* **273**(24), 1289–1297 (1965).
14. N. P. Whitehead, C. Pham, O. L. Gervasio, and D. G. Allen, "N-Acetylcysteine ameliorates skeletal muscle pathophysiology in mdx mice," *J. Physiol.* **586**(7), 2003–2014 (2008).
15. C. E. Woods, D. Novo, M. DiFranco, J. Capote, and J. L. Vergara, "Propagation in the transverse tubular system and voltage dependence of calcium release in normal and mdx mouse muscle fibres," *J. Physiol.* **568**(3), 867–880 (2005).
16. M. DiFranco, C. E. Woods, J. Capote, and J. L. Vergara, "Dystrophic skeletal muscle fibers display alterations at the level of calcium microdomains," *Proc. Natl. Acad. Sci. U.S.A.* **105**(38), 14698–14703 (2008).
17. R. M. Lovering, L. Michaelson, and C. W. Ward, "Malformed mdx myofibers have normal cytoskeletal architecture yet altered EC coupling and stress-induced Ca2+ signaling," *Am. J. Physiol. Cell Physiol.* **297**(3), C571–C580 (2009).
18. J. Capote, M. DiFranco, and J. L. Vergara, "Excitation-contraction coupling alterations in mdx and utrophin/dystrophin double knockout mice: a comparative study," *Am. J. Physiol. Cell Physiol.* **298**(5), C1077–C1086 (2010).
19. E. Clarkson, C. F. Costa, and L. M. Machesky, "Congenital myopathies: diseases of the actin cytoskeleton," *J. Pathol.* **204**(4), 407–417 (2004).
20. O. Friedrich, M. Both, C. Weber, S. Schürmann, M. D. H. Teichmann, F. von Wegner, R. H. A. Fink, M. Vogel, J. S. Chamberlain, and C. Garbe, "Microarchitecture Is Severely Compromised but Motor Protein Function Is Preserved in Dystrophic mdx Skeletal Muscle," *Biophys. J.* **98**(4), 606–616 (2010).
21. N. G. Laing and K. J. Nowak, "When contractile proteins go bad: the sarcomere and skeletal muscle disease," *Bioessays* **27**(8), 809–822 (2005).
22. S. Lange, F. Xiang, A. Yakovenko, A. Vihola, P. Hackman, E. Rostkova, J. Kristensen, B. Brandmeier, G. Franzen, B. Hedberg, L. G. Gunnarsson, S. M. Hughes, S. Marchand, T. Sejersen, I. Richard, L. Edström, E. Ehler, B. Udd, and M. Gautel, "The kinase domain of titin controls muscle gene expression and protein turnover," *Science* **308**(5728), 1599–1603 (2005).
23. L. Edström, L. E. Thornell, J. Albo, S. Landin, and M. Samuelsson, "Myopathy with respiratory failure and typical myofibrillar lesions," *J. Neurol. Sci.* **96**(2-3), 211–228 (1990).
24. P. J. Campagnola and L. M. Loew, "Second-harmonic imaging microscopy for visualizing biomolecular arrays in cells, tissues and organisms," *Nat. Biotechnol.* **21**(11), 1356–1360 (2003).
25. W. R. Zipfel, R. M. Williams, and W. W. Webb, "Nonlinear magic: multiphoton microscopy in the biosciences," *Nat. Biotechnol.* **21**(11), 1369–1377 (2003).
26. X. Y. Chen, O. Nadiarynkh, S. Plotnikov, and P. J. Campagnola, "Second harmonic generation microscopy for quantitative analysis of collagen fibrillar structure," *Nat. Protoc.* **7**(4), 654–669 (2012).
27. F. Tiaho, G. Recher, and D. Rouède, "Estimation of helical angles of myosin and collagen by second harmonic generation imaging microscopy," *Opt. Express* **15**(19), 12286–12295 (2007).
28. P. J. Campagnola, A. C. Millard, M. Terasaki, P. E. Hoppe, C. J. Malone, and W. A. Mohler, "Three-dimensional high-resolution second-harmonic generation imaging of endogenous structural proteins in biological tissues," *Biophys. J.* **82**(1), 493–508 (2002).
29. F. Vanzi, M. Capitanio, L. Sacconi, C. Stringari, R. Cicchi, M. Canepari, M. Maffei, N. Piroddi, C. Poggesi, V. Nucciotti, M. Linari, G. Piazzesi, C. Tesi, R. Antolini, V. Lombardi, R. Bottinelli, and F. S. Pavone, "New techniques in linear and non-linear laser optics in muscle research," *J. Muscle Res. Cell Motil.* **27**(5-7), 469–479 (2006).
30. S. V. Plotnikov, A. M. Kenny, S. J. Walsh, B. Zubrowski, C. Joseph, V. L. Scranton, G. A. Kuchel, D. Dauser, M. Xu, C. C. Pilbeam, D. J. Adams, R. P. Dougherty, P. J. Campagnola, and W. A. Mohler, "Measurement of muscle disease by quantitative second-harmonic generation imaging," *J. Biomed. Opt.* **13**(4), 044018 (2008).
31. F. Légaré, C. Pfeffer, and B. R. Olsen, "The role of backscattering in SHG tissue imaging," *Biophys. J.* **93**(4), 1312–1320 (2007).
32. E. Ralston, B. Swaim, M. Czapiga, W. L. Hwu, Y. H. Chien, M. G. Pittis, B. Bembli, O. Schwartz, P. Plotz, and N. Raben, "Detection and imaging of non-contractile inclusions and sarcomeric anomalies in skeletal muscle by second harmonic generation combined with two-photon excited fluorescence," *J. Struct. Biol.* **162**(3), 500–508 (2008).
33. C. Odin, T. Guilbert, A. Alkilani, O. P. Boryskina, V. Fleury, and Y. Le Grand, "Collagen and myosin characterization by orientation field second harmonic microscopy," *Opt. Express* **16**(20), 16151–16165 (2008).
34. M. Both, M. Vogel, O. Friedrich, F. von Wegner, T. Künsting, R. H. A. Fink, and D. Uttenweiler, "Second harmonic imaging of intrinsic signals in muscle fibers in situ," *J. Biomed. Opt.* **9**(5), 882–892 (2004).

35. C. Greenhalgh, N. Prent, C. Green, R. Cisek, A. Major, B. Stewart, and V. Barzda, "Influence of semicrystalline order on the second-harmonic generation efficiency in the anisotropic bands of myocytes," *Appl. Opt.* **46**(10), 1852–1859 (2007).
36. G. Recher, D. Rouède, P. Richard, A. Simon, J.-J. Bellanger, and F. Tiaho, "Three distinct sarcomeric patterns of skeletal muscle revealed by SHG and TPEF Microscopy," *Opt. Express* **17**(22), 19763–19777 (2009).
37. V. Nucciotti, C. Stringari, L. Sacconi, F. Vanzi, L. Fusi, M. Linari, G. Piazzesi, V. Lombardi, and F. S. Pavone, "Probing myosin structural conformation in vivo by second-harmonic generation microscopy," *Proc. Natl. Acad. Sci. U.S.A.* **107**(17), 7763–7768 (2010).
38. S. Psilodimitrakopoulos, V. Petegnief, G. Soria, I. Amat-Roldan, D. Artigas, A. M. Planas, and P. Loza-Alvarez, "Estimation of the effective orientation of the SHG source in primary cortical neurons," *Opt. Express* **17**(16), 14418–14425 (2009).
39. M. E. Llewellyn, R. P. J. Barretto, S. L. Delp, and M. J. Schnitzer, "Minimally invasive high-speed imaging of sarcomere contractile dynamics in mice and humans," *Nature* **454**(7205), 784–788 (2008).
40. G. Recher, D. Rouède, E. Schaub, and F. Tiaho, "Skeletal muscle sarcomeric SHG patterns photo-conversion by femtosecond infrared laser," *Biomed. Opt. Express* **2**(2), 374–384 (2011).
41. S. I. Santos, M. Mathew, O. E. Olarte, S. Psilodimitrakopoulos, and P. Loza-Alvarez, "Femtosecond laser axotomy in *Caenorhabditis elegans* and collateral damage assessment using a combination of linear and nonlinear imaging techniques," *PLoS ONE* **8**(3), e58600 (2013).
42. D. Rouède, J.-J. Bellanger, G. Recher, and F. Tiaho, "Study of the effect of myofibrillar misalignment on the sarcomeric SHG intensity pattern," *Opt. Express* **21**(9), 11404–11414 (2013).
43. G. Recher, D. Rouède, C. Tascon, L. A. D'Amico, and F. Tiaho, "Double-band sarcomeric SHG pattern induced by adult skeletal muscles alteration during myofibrils preparation," *J. Microsc.* **241**(2), 207–211 (2011).
44. L. Moreaux, O. Sandre, S. Charpak, M. Blanchard-Desce, and J. Mertz, "Coherent scattering in multi-harmonic light microscopy," *Biophys. J.* **80**(3), 1568–1574 (2001).
45. D. Rouède, J.-J. Bellanger, E. Schaub, G. Recher, and F. Tiaho, "Theoretical and Experimental SHG Angular Intensity Patterns from Healthy and Proteolysed Muscles," *Biophys. J.* **104**(9), 1959–1968 (2013).
46. D. Rouède, G. Recher, J. J. Bellanger, M. T. Lavault, E. Schaub, and F. Tiaho, "Modeling of Supramolecular Centrosymmetry Effect on Sarcomeric SHG Intensity Pattern of Skeletal Muscles," *Biophys. J.* **101**(2), 494–503 (2011).
47. B. R. Klyen, T. Shavlakadze, H. G. Radley-Crabb, M. D. Grounds, and D. D. Sampson, "Identification of muscle necrosis in the mdx mouse model of Duchenne muscular dystrophy using three-dimensional optical coherence tomography," *J. Biomed. Opt.* **16**(7), 076013 (2011).
48. V. Dubowitz and C. A. Sewry, *Muscle Biopsy: A Practical Approach, Third Edition* (London, 2007).
49. B. M. Millman, "The filament lattice of striated muscle," *Physiol. Rev.* **78**(2), 359–391 (1998).
50. D. Rhee, J. M. Sanger, and J. W. Sanger, "The premyofibril: evidence for its role in myofibrillogenesis," *Cell Motil. Cytoskeleton* **28**(1), 1–24 (1994).
51. J. W. Sanger, J. S. Wang, B. Holloway, A. P. Du, and J. M. Sanger, "Myofibrillogenesis in Skeletal Muscle Cells in Zebrafish," *Cell Motil. Cytoskeleton* **66**(8), 556–566 (2009).
52. J. K. Y. U. Hiroko Yokota, "Optical Second Harmonic Generation Microscopy as a Tool of Material Diagnosis," *Phys. Res. Int.* **2012**, 12 (2012).
53. M. Rivard, C.-A. Couture, A. K. Miri, M. Laliberté, A. Bertrand-Grenier, L. Mongeau, and F. Légaré, "Imaging the bipolarity of myosin filaments with Interferometric Second Harmonic Generation microscopy," *Biomed. Opt. Express* **4**(10), 2078–2086 (2013).
54. X. Wang, N. Weisleder, C. Collet, J. Zhou, Y. Chu, Y. Hirata, X. Zhao, Z. Pan, M. Brotto, H. Cheng, and J. Ma, "Uncontrolled calcium sparks act as a dystrophic signal for mammalian skeletal muscle," *Nat. Cell Biol.* **7**(5), 525–530 (2005).
55. D. G. Allen, N. P. Whitehead, and E. W. Yeung, "Mechanisms of stretch-induced muscle damage in normal and dystrophic muscle: role of ionic changes," *J. Physiol.* **567**(3), 723–735 (2005).
56. L. S. Song, E. A. Sobie, S. McCulle, W. J. Lederer, C. W. Balke, and H. Cheng, "Orphaned ryanodine receptors in the failing heart," *Proc. Natl. Acad. Sci. U.S.A.* **103**(11), 4305–4310 (2006).
57. F. R. Heinzel, V. Bitto, L. Biesmans, M. Wu, E. Detre, F. von Wegner, P. Claus, S. Dymarkowski, F. Maes, J. Bogaert, F. Rademakers, J. D'hooge, and K. Sipido, "Remodeling of T-tubules and reduced synchrony of Ca²⁺ release in myocytes from chronically ischemic myocardium," *Circ. Res.* **102**(3), 338–346 (2008).
58. K. M. Dibb, J. D. Clarke, M. A. Horn, M. A. Richards, H. K. Graham, D. A. Eisner, and A. W. Trafford, "Characterization of an extensive transverse tubular network in sheep atrial myocytes and its depletion in heart failure," *Circ Heart Fail* **2**(5), 482–489 (2009).
59. A. R. Lyon, K. T. MacLeod, Y. Zhang, E. Garcia, G. K. Kanda, M. J. Lab, Y. E. Korchev, S. E. Harding, and J. Gorelik, "Loss of T-tubules and other changes to surface topography in ventricular myocytes from failing human and rat heart," *Proc. Natl. Acad. Sci. U.S.A.* **106**(16), 6854–6859 (2009).
60. S. Wei, A. Guo, B. Chen, W. Kutschke, Y. P. Xie, K. Zimmerman, R. M. Weiss, M. E. Anderson, H. Cheng, and L. S. Song, "T-tubule remodeling during transition from hypertrophy to heart failure," *Circ. Res.* **107**(4), 520–531 (2010).
61. Z. Li, E. Colucci-Guyon, M. Pinçon-Raymond, M. Mericskay, S. Pournin, D. Paulin, and C. Babinet, "Cardiovascular lesions and skeletal myopathy in mice lacking desmin," *Dev. Biol.* **175**(2), 362–366 (1996).

62. Z. Li, M. Mericskay, O. Agbulut, G. Butler-Browne, L. Carlsson, L. E. Thornell, C. Babinet, and D. Paulin, "Desmin is essential for the tensile strength and integrity of myofibrils but not for myogenic commitment, differentiation, and fusion of skeletal muscle," *J. Cell Biol.* **139**(1), 129–144 (1997).
 63. R. M. Lovering, A. O'Neill, J. M. Muriel, B. L. Prosser, J. Strong, and R. J. Bloch, "Physiology, structure, and susceptibility to injury of skeletal muscle in mice lacking keratin 19-based and desmin-based intermediate filaments," *Am. J. Physiol. Cell Physiol.* **300**(4), C803–C813 (2011).
-

1. Introduction

Duchenne muscular dystrophy (DMD) is a devastating X-linked myopathy affecting 1 in 3500 boys. Despite the broad, systemic pathophysiology of DMD, the primary defect is mutation of the dystrophin gene, which encodes a membrane-associated protein found primarily in skeletal muscle [1–3]. The lack of dystrophin induces a complete destruction of subsarcolemmal glyco-protein complexes resulting in skeletal and cardiac progressive myonecrosis with associated progressive fibrosis. As a consequence, the pathology of DMD involves skeletal muscle weakness, inflammation, increased fatigability, cardiomyopathy, fibrosis and premature death due to cardio-respiratory failure [4]. The pathogenesis of DMD is frequently studied in the dystrophic mdx mouse genetically selected for a point mutation on exon 23 of the DMD gene [5]. Mdx mice are completely deficient in dystrophin protein. They are histopathologically characterized by mild myo-necrosis due to their greater muscular regenerative property and mild fibrosis. As a consequence, mdx mice have a near normal lifespan. Despite milder muscular histopathological defect compared to DMD, mdx mouse is considered a good model in which to study the muscle regeneration-degeneration mechanism [6, 7]. In mdx mouse model, eccentric contractions enhanced force loss due to myofibrillar impairment [8]. Calcium entry through stretch-dependent ion channels [9, 10] and intracellular elevation of free calcium result in increased protein degradation [11]. At ultrastructural level, sarcomere with A-band slippage and myofibrillar disruptions due to titin and desmin destructions has been described for dystrophic muscle [12]. Before the identification of dystrophin mutations as the cause of DMD, early investigators speculated that DMD could result, at least in part, from oxidative stress experienced by muscle based on similarities with muscle pathology that occurred in vitamin E deficiency [13] and it is suggested that free radicals are involved in the pathophysiology of muscular dystrophy [4]. Furthermore, it has been shown that early antioxidant treatment with N-Acetylcysteine ameliorates skeletal muscle pathophysiology in mdx mice [14]. Excitation contraction disruption has been suggested as a cue of muscle weakness in mdx mouse [15–18]. More importantly, genetic defects of several sarcomeric and cytoskeletal protein of human and animal model involve structural sarcomeric and myofibrillar disorganization [19–23].

SHG microscopy is a powerful tool to image intrinsic subcellular signals from endogenous well-ordered proteins such as tubulin, myosin and collagen [24–27]. Concerning myosin, coherent emission from myosin molecules of thick filaments is responsible of the characteristic periodical sarcomeric SHG signal observed in striated muscles [28–39]. We have previously shown that the canonical single frequency (1f) sarcomeric SHG intensity pattern (SHG-IP) is converted to double frequency (2f) sarcomeric SHG-IP in xenopus muscle when concentration of reactive oxygen species (ROS) increases [40]. Since mdx muscular dystrophy is characterized by an increase in free radicals [4], we hypothesize that muscle damage and degradation in mdx mouse could be the result of muscle oxidation leading to conversion from 1f to 2f sarcomeric SHG-IP with appearance of Y- or vernier-shape optical anomalies [20, 32, 34, 36, 41]. These anomalies have been interpreted as the possible result of myofibrillar deformation or change of myosin orientation between different arms of the Y- or vernier-shape [20]. However, from polarization study, we have previously shown that orientation of myosin is unchanged in all branches of the Y-shape sarcomeric SHG-IP in experimentally proteolysed muscle tissues [36, 40]. Moreover, in a recent work concerning proteolysed muscle tissue, we gave evidence that myofibrillar misalignment is responsible of such optical defects [42]. Therefore, the mechanism underlying change of SHG-IP in mdx

muscle needs to be elucidated. The main goal of the present work is to demonstrate that 2f sarcomeric SHG-IP is the result of myofibrillar misalignment in mdx muscles. To this aim, SHG, two-photon excitation fluorescence (TPEF), SHG angular intensity pattern (SHG-AIP) and transmission electron microscopy (TEM) imaging have been used. Whereas SHG signal is emitted by sarcomeric A-bands, fluorescence signal originates from immunodetection of α -actinin (a molecular marker of sarcomeric Z-lines) or lipophilic fluorescent dye (a molecular marker of I-band tubular system and triads). We found 1/ a significant increase of 2f sarcomeric SHG-IPs in pathological mdx versus control (BL10) tissues 2/ a good spatial correlation between 2f sarcomeric SHG- and TPEF-IPs 3/ a drastic localized increase in 2f sarcomeric SHG-IPs inside preserved fibers near necrotic regions. In mdx muscle, experimental SHG-AIPs with one centered spot are predominantly (>90%) correlated to 2f sarcomeric SHG-IP putting forward that 2f sarcomeric SHG-IP is well the result of myofibrillar displacement in mdx muscle. At ultrastructural TEM level, myofibrillar misalignments are also observed and are predominantly found inside preserved fibers near necrotic regions showing their spatial correlation with 2f sarcomeric SHG-IPs. We also found a reduction of triads in regions of myofibrillar misalignment, suggesting excitation contraction disruption. From theoretical simulation, we point out the close correlation between 2f sarcomeric SHG-IP and myofibrillar displacement demonstrating that Y- and vernier-shape SHG-IPs are optical illusions of myofibrillar misalignment. From these simulations, we analyze and discuss the contribution of different myofibrillar arrangements to the appearance of 2f sarcomeric SHG-IPs in muscle tissue. We conclude that 2f sarcomeric SHG-IPs observed in mdx muscles are a signature of muscle damage due to myofibrillar displacement and triads rupture.

2. Materials and methods

2.1. Tissue preparation

Six wild-type (BL10) mice and six mdx (mouse model of Duchenne muscular dystrophy) animals were provided by Pr. Y. Cherel (ENV, ONIRIS, Nantes, France). All the mice performed 4 minutes swimming exercises 3 times before euthanasia. Swimming exercises were scheduled at D-4 afternoon, D-3 morning and D-3 afternoon. Mice were anesthetized and then euthanized by cervical dislocation. Gastrocnemius muscles of wild-type and mdx mouse were quickly dissected in ice cold phosphate-buffered saline (PBS). A first group of muscles were immediately fixed with 4% PFA-PBS at slack length. A second group of muscle were stretched to 110% of their slack length and tied to rigid plastic rod for 4 hours in PBS saline at room temperature (18-22°C) before fixation with 4% PFA-PBS. Muscles of the second group were used for SHG-AIP experiments. The immediate fixative procedure was previously shown to prevent spontaneous muscle proteolysis [43] and 4 hours elongated muscle were found to induced mild proteolysis at room temperature (18-22°C) [42]. Muscles were kept overnight at 4°C in the fixative then washed several times in the PBS. Dissected pieces (200–400 μ m thickness) of muscle fibers were mounted in a POC-R2 tissue culture chamber system (PeCon, Erbach, Germany) in PBS and stabilized between two coverslips.

For α -actinin immunofluorescence labeling, 8 μ m cryostat sections of prefixed muscles were mounted on gelatin coated coverslips, permeabilized with buffer containing 0.5% triton and 5% fetal calf serum for 10 minutes and incubated at 4°C overnight in PBS containing 0.1% triton, 5% fetal calf serum and α -actinin antibody (1:100, mouse monoclonal IgM, ab9465, Abcam, Cambridge, MA, USA). Slices were rinsed three times in PBS and incubated at 4°C overnight in PBS containing 0.1% triton, 5% fetal calf serum and secondary antibody (1:100, Alexa Fluor 488 goat antimouse IgG, A11029, Molecular Probes, Eugene, OR, USA). After being rinsed three times, the tissue was covered with a drop of mounting medium (Vectashield, Vector Burlingame, CA) and a second coverslip was laid on. After being sealed, preparations were imaged.

For fluorescent labeling, dissected pieces (200-400 μm thickness) of muscle fibers were incubated with PBS containing 50 μM of RS19 overnight. RS19 is a lipophilic dye analog of the voltage sensitive dye Di-6-ASPBS [44] and is provided by Dr M. Blanchard-Desce (UMR CNRS 5255, University of Bordeaux, France). Muscle fibers were rinsed with PBS overnight before TPEF imaging.

For transmission electron microscopy (TEM), blocs of approximately 1 mm^3 from 2 control and 2 mdx mice were cut from PFA-prefixed and PBS-washed gastrocnemius muscles and further fixed in glutaraldehyde (2.5%, 4°C, in 0.2 M cacodylate buffer, pH 7.2) for one hour. Blocs were washed in cacodylate buffer. The next day, they were post-fixed in osmium tetroxide (2%) for one hour and washed with cacodylate buffer. On the following day, they were dehydrated in a graded acetone series. The day after, they were impregnated firstly into a mix of Epon, Araldite and acetone during one hour and a half, and secondly into a mix of Epon, Araldite and DMP30. Samples were then laid down into molds and polymerization occurred overnight at 60°C. Blocs were then desiccated during 24 hours and mounted on the cutting stage. Ultra fine slices were made with an ultra-microtome (Ultracut E, Reichert) and mounted on a copper grid before being stained with uranyl acetate (2.5%) during one hour. They were then dipped in lead citrate and finally rinsed. Imaging was performed using a JEOL 100CXII microscope at 80 kV accelerating voltage, at the TEM mRIC platform (<http://microscopie.univ-rennes1.fr/>).

2.2. SHG and TPEF imaging system

SHG and TPEF images were acquired on platform PIXEL (<http://pixel.univ-rennes1.fr/>), facility of GIS EUROPIA, University of Rennes1, France. The SHG imaging system is described elsewhere [45]. Briefly, it consists in a confocal Leica TCS SP2 scanning head (Leica Microsystems, Mannheim, Germany) mounted on a Leica DMIRE2 inverted microscope and equipped with a MAITAI Spectra Physics femtosecond laser (Spectra Physics, Santa Clara, CA, USA). High NA water immersion objective (Olympus LUMFL 60W \times 1.1 NA) (Olympus, Tokyo, Japan) was used for applying 10-20 mW of 940 nm excitation at the sample. SHG signal was collected in the forward direction using a multi-immersion condenser (Leica S1 NA = 0.9-1.4). BG39 band pass and 470 nm IR (10 nm FWHM) filters were placed before the PMT. All specimens were positioned on the fixed x, y stage of the microscope with an incident laser beam propagating along z direction. In order to obtain SHG-AIP of each pixel of a SHG image, the aperture diaphragm was removed from the condenser and replaced by a movable dark screen with a pinhole in its plane (see reference [45] for details). SHG-AIP is obtained by acquisition of the same field of view moving the pinhole over the entire field of the aperture diaphragm. Each SHG-AIP is obtained for 7×7 positions of the pinhole with angular width of 10° . Acquisition time for each position is ten seconds. Open source ImageJ software (<http://rsb.info.nih.gov/ij/>) was used to quantify 2f sarcomeric SHG-IP as previously reported [36]. MATLAB (MathWorks, Natick, MA, USA) was used to plot the corresponding experimental SHG-AIP.

2.3. Theoretical simulation

Calculation of the SHG intensity emitted by a bundle of myofibrils has been done elsewhere [42, 45, 46]. Briefly, far field SHG intensity $I_{2\omega}(\theta, \varphi)$ emitted in unit solid angle $d\Omega = \sin \theta d\theta d\varphi$ is given by [42]

$$I_{2\omega}(\theta, \varphi) = \left| \int e^{-i(k_x^{2\omega}x + k_y^{2\omega}y + k_z^{2\omega}z)} M(x, y, z) e^{-2\frac{x^2+y^2}{w_{xy}^2} - 2\frac{z^2}{w_z^2} + 2i\xi k_z^{\omega}z} dx dy dz \right|^2 \quad (1)$$

where summation is made over all nonlinear sources located at x, y, z in the muscular tissue, assuming that the incident laser beam propagates in z direction and that the excitation field is 3D Gaussian at the vicinity of the focus. Constant coefficients and polarization dependence of the SHG signal are factorizable factors and are not taken into account. $\mathbf{k}^\omega = k^\omega(0,0,1)$ and $\mathbf{k}^{2\omega} = k^{2\omega}(\sin\theta\cos\varphi, \sin\theta\sin\varphi, \cos\theta)$ are wave vectors of respectively fundamental and harmonic waves written in laboratory coordinates x, y, z . $M(x, y, z)$ is the spatial modulation of the second-order nonlinear optical susceptibility defined by $\chi^{(2)}(x, y, z) = M(x, y, z) \times \chi^{(2)}$. $\xi = 1 - (k^\omega z_r)^{-1}$ and $z_r = \pi n_\omega w_{xy}^2 \lambda_\omega^{-1}$ is the Rayleigh range. Considering identical adjacent myofibrils parallel to x direction and of rectangular size in y and z directions, Eq. (1) can be rewritten

$$I_{2\omega}(\theta, \varphi) = \left| \sum_f \left(\int e^{-ik_x^2 x} M_x^f(x) e^{-\frac{2x^2}{w_x^2}} dx \int e^{-ik_y^2 y} M_y^f(y) e^{-\frac{2y^2}{w_y^2}} dy \int e^{-ik_z^2 z} M_z^f(z) e^{-\frac{2z^2}{w_z^2} + 2i\xi k_z^2 z} dz \right) \right|^2 \quad (2)$$

where summation is made over all myofibrils f and where $M_\eta^f(\eta)$ is the spatial modulation of the second-order nonlinear optical susceptibility for myofibril f in η direction ($\eta = x, y, z$). $M_y^f = M_z^f = 1$ within each myofibril and $M_y^f = M_z^f = 0$ elsewhere. $M_x^f = +1$ or -1 in the A-band region of each sarcomere and $M_x^f = 0$ elsewhere. Sign inversion takes into account myosin thick filament polarity inversion at the M-band. Using a development in Fourier series of M_η^f with spatial period L_η ($\eta = x, y, z$), $M_\eta^f(\eta) = \sum_{n \in \mathbb{Z}} c_{\eta n}^f e^{2i\pi n L_\eta^{-1} \eta}$, Eq. (2) results in

$$I_{2\omega}(\mathbf{r}) = u \left| \sum_f \left(\sum_{n \in \mathbb{Z}} c_{xn}^f e^{-\frac{1}{4} w_x^2 (k_x^{2\omega} - 2\pi n L_x^{-1})^2} \sum_{n \in \mathbb{Z}} c_{yn}^f e^{-\frac{1}{4} w_y^2 (k_y^{2\omega} - 2\pi n L_y^{-1})^2} \sum_{n \in \mathbb{Z}} c_{zn}^f e^{-\frac{1}{4} w_z^2 (k_z^{2\omega} - 2\xi k_z^\omega - 2\pi n L_z^{-1})^2} \right) \right|^2, \quad (3)$$

with $u = \left(\frac{\pi}{2}\right)^3 w_{xy}^4 w_z^2$. $L_x = L$ is the sarcomere size and $L_y = L_z$ have to be chosen greater than the size of the bundle of myofibrils in y and z directions. Fourier coefficient $c_{\eta n}^f = L_\eta^{-1} \int_{-L_\eta/2}^{L_\eta/2} M_\eta^f(\eta) e^{-2i\pi n L_\eta^{-1} \eta} d\eta$ is given by

$$\begin{cases} c_{xn}^f &= \frac{2i}{\pi n} \sin\left(\frac{1}{2} \pi n L_x^{-1} (A - m)\right) \times \sin\left(\frac{1}{2} \pi n L_x^{-1} (A + m)\right) \times \exp(-2i \pi n L_x^{-1} \Delta_x^f), \quad n \in \mathbb{Z}^* \\ &= 0, \quad n = 0 \\ c_{\eta n}^f &= \frac{1}{\pi n} \sin(\pi n L_\eta^{-1} \ell_\eta) \times \exp(-2i \pi n L_\eta^{-1} \Delta_\eta^f), \quad n \in \mathbb{Z}^*, \quad \eta = y, z \\ &= \ell_\eta L_\eta^{-1}, \quad n = 0, \quad \eta = y, z \end{cases} \quad (4)$$

A and m are sizes of the A- and M-bands respectively and ℓ_y and ℓ_z are sizes of each myofibril in respectively y and z directions (see the schematic view of the sarcomere in the inset of Fig. 6). Δ_η^f is a coefficient that is introduced to take account of a displacement of the center of the focus spot with respect to the center of the sarcomere in η direction ($\eta = x, y, z$) for each myofibril f .

α -actinin TPEF intensity $I_{TPEF}(x, y, z)$ produced at position x, y, z in the muscular tissue is driven by the convolution product of the Alexa Fluor dye concentration $C(x, y, z)$ by the square of the Gaussian intensity of the incident IR beam

$$\mathbf{I}_{TPEF}(x, y, z) = \int e^{-4\left(\frac{x_0^2 + y_0^2 + z_0^2}{w_{xy}^2 + w_z^2}\right)} C(x_0 - x, y_0 - y, z_0 - z) dx_0 dy_0 dz_0. \quad (5)$$

Decomposition over all myofibrils f leads to

$$\mathbf{I}_{TPEF}(x, y, z) = \sum_f \left(\int e^{-4\frac{x_0^2}{w_{xy}^2}} C_x^f(x_0 - x) dx_0 \int e^{-4\frac{y_0^2}{w_{xy}^2}} C_y^f(y_0 - y) dy_0 \int e^{-4\frac{z_0^2}{w_z^2}} C_z^f(z_0 - z) dz_0 \right), \quad (6)$$

where C_η^f is the dye concentration of myofibril f in η direction ($\eta = x, y, z$). $C_y^f = C_z^f = 1$ within each myofibril and $C_y^f = C_z^f = 0$ elsewhere. $C_x^f = 1$ for the dye labeled region at the Z line of each sarcomere and $C_x^f = 0$ elsewhere. Using again a development in Fourier series of C_η^f with the same Fourier spatial periods L_η as before, $C_\eta^f(\eta) = \sum_{n \in \mathbb{Z}} d_{\eta n}^f e^{2i\pi n L_\eta^{-1} \eta}$ ($\eta = x, y, z$), Eq. (6) results in

$$\mathbf{I}_{TPEF}(x, y, z) = v \sum_f \left(\sum_{n \in \mathbb{Z}} d_{xn}^f e^{-\frac{1}{4} w_{xy}^2 \pi^2 n^2 L_x^2} \sum_{m \in \mathbb{Z}} d_{ym}^f e^{-\frac{1}{4} w_{xy}^2 \pi^2 m^2 L_y^2} \sum_{p \in \mathbb{Z}} d_{zn}^f e^{-\frac{1}{4} w_z^2 \pi^2 n^2 L_z^2} \right), \quad (7)$$

with $v = \frac{1}{8} \pi^{3/2} w_{xy}^2 w_z$ and Fourier coefficient $d_{\eta n}^f = L_\eta^{-1} \int_{-L_\eta/2}^{L_\eta/2} C_\eta^f(\eta) e^{-2i\pi n L_\eta^{-1} \eta} d\eta$ given by

$$\left| \begin{aligned} d_{\eta n}^f &= \frac{1}{\pi n} \sin(\pi n L_\eta^{-1} \ell_\eta) \times \exp(-2i\pi n L_\eta^{-1} \Delta_\eta^f), & n \in \mathbb{Z}^*, & (\eta = x, y, z) \\ &= \ell_\eta L_\eta^{-1}, & n = 0, & (\eta = x, y, z) \end{aligned} \right. \quad (8)$$

ℓ_y, ℓ_z are still sizes of each myofibril in respectively y and z directions and ℓ_x is size of the dye labeled region at the Z-line in x direction. Δ_η^f is a coefficient that takes account here for the displacement of the center of the focus spot with respect to the center of the dye labeled region at the Z-line in η direction ($\eta = x, y, z$) for each myofibril f .

MATLAB (MathWorks, Natick, MA, USA) was used for the calculation of theoretical SHG-AIP and -IP given respectively by Eq. (3) and by angular integration of Eq. (3) over the condenser aperture using $u = 1$ (see reference [42] for details). Equation (7) is used for calculation of theoretical TPEF-IP using $v = 1$. Spatial periods of the Fourier development series are $L_x = L = 2 \mu m$, the experimental sarcomere size and $L_y = L_z = 15 \mu m$. Number of Fourier coefficients is set to $n = 40$ [45]. Sizes of sarcomeric A- and M-bands for well ordered thick filaments within each sarcomere are respectively $A = 1.6 \mu m$ and $m = 150 \text{ nm}$. $\ell_y = \ell_z = 1 \mu m$ and size of the dye labeled region at the Z-line in x direction is arbitrary set to $\ell_x = 100 \text{ nm}$. $k^\omega = 2\pi n_\omega \lambda_\omega^{-1}$, $k^{2\omega} = 2\pi n_{2\omega} \lambda_{2\omega}^{-1}$, $\lambda_\omega = 940 \text{ nm}$ and $n_\omega = n_{2\omega} = 1.33$. $w_{xy} = 0.48 \mu m$ and $w_z = 2.4 \mu m$ were estimated from the two-photon excitation PSF obtained from $0.17 \mu m$ diameter fluorescent micro beads (see reference [42] for details).

3. Experimental results

Duplex SHG and α -actinin-based TPEF imaging of mouse control (BL10) and mdx gastrocnemius muscle tissues are illustrated in Fig. 1.

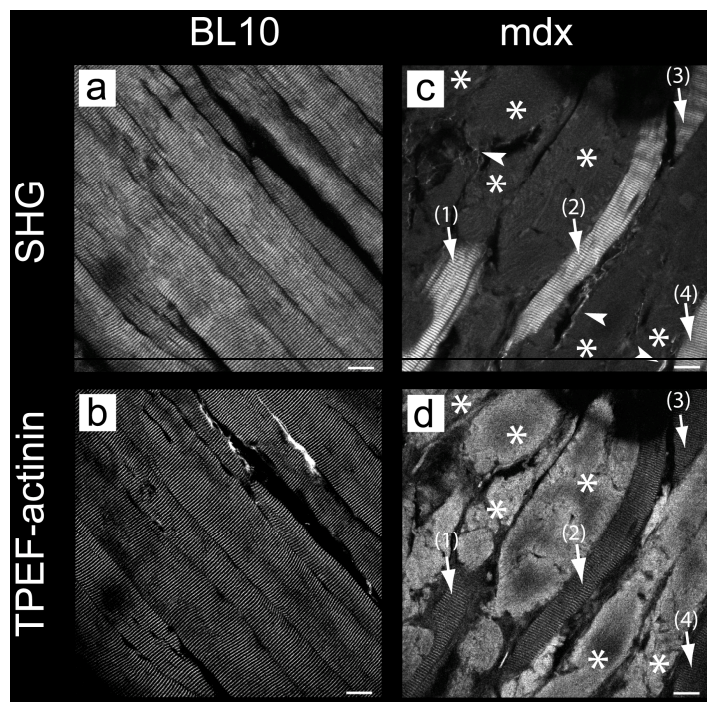


Fig. 1. Optical XY sections illustrating duplex SHG (a,c) and TPEF α -actinin (b,d) images from control BL10 gastrocnemius (a,b) and mdx gastrocnemius (c,d) mouse muscles. Note that in both TPEF and SHG images, necrotic fibers (asterisks) lacked the canonical sarcomeric banding pattern of preserved fibers (arrows). Whereas these regions of necrosis are the brightest in TPEF images due to non-specific accumulation of secondary fluorescently labeled antibodies, the opposite is observed for SHG images due to proteolysis and degradation of myosin filaments. Note also for SHG images the bright filaments (arrowheads) reminiscent of collagen fibrils surrounding necrotic fibers. Scale bar = 20 μ m.

Fluorescence is emitted from immunodetection of α -actinin, a molecular marker of sarcomeric Z-lines [36, 42]. As expected, control muscle tissue is characterized by bright SHG (Fig. 1(a)) and TPEF (Fig. 1(b)) signals delineating each myofiber. In contrast to control, SHG (Fig. 1(c)) and TPEF (Fig. 1(d)) images of mdx muscle often show necrotic or degenerating cluster of muscle fibers (asterisks) separating well-preserved fibers (numbered arrows) in agreement with the general histological feature of necrotic mdx muscle [3, 47]. For the SHG image of mdx muscle (Fig. 1(c)), portion of 4 preserved fibers are indicated by bright SHG signal (arrows) bordered by necrotic fibers with drastically reduced SHG signal (asterisks). A close look at the necrotic fiber regions reveals the presence of collagen filaments that generate SHG signal (arrowheads). For the TPEF image of mdx muscle (Fig. 1(d)), necrotic fibers are brighter than the preserved myofibers since the former behave as sponge that none specifically trapped both the primary and secondary antibodies as recently shown in mdx mouse [47]. At higher magnification, canonical 1f sarcomeric IPs are predominantly seen in preserved fibers in both SHG (Fig. 2(a)) and TPEF (Fig. 2(b)) images of mdx muscle.

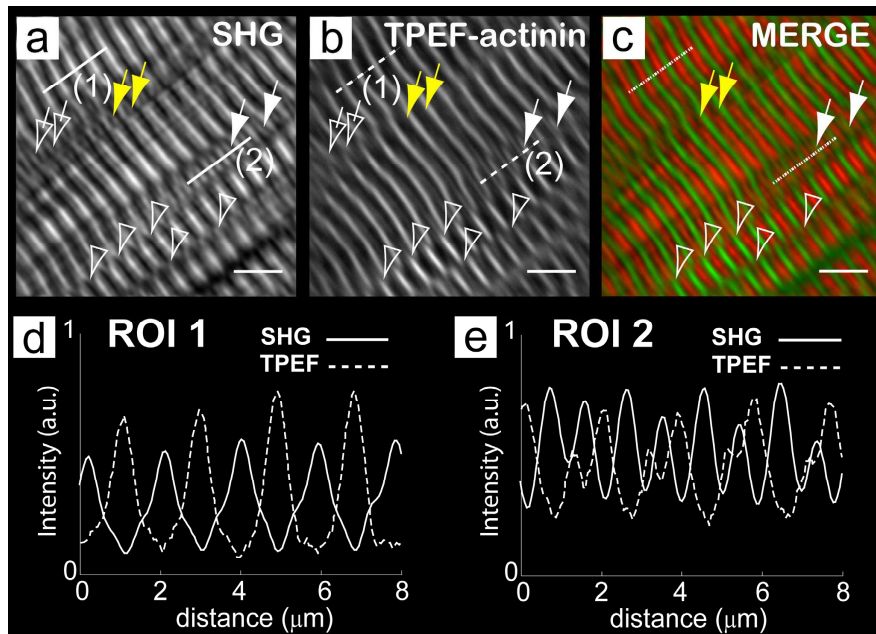


Fig. 2. Typical duplex SHG (a), TPEF (b) and merge image (c) inside preserved myofiber of mdx mouse gastrocnemius muscle. Note that for the merge image, SHG and TPEF signals are respectively in red and green color. Note also that in (a, b and c) white arrowheads and empty or filled white arrows all indicate 2f sarcomeric TPEF-IPs spatially correlated to 2f sarcomeric SHG-IPs whereas yellow filled arrows indicate 1f sarcomeric TPEF-IPs spatially correlated to 2f sarcomeric SHG-IPs. (d,e) Pixel grey level intensity profile of SHG (full lines) and TPEF (dotted lines) signals along indicated lines in images (a), (b) and (c). Scale bar = 5 μm .

A close look at the merge signal (Fig. 2(c)) and at the intensity profile plot (Fig. 2(d)) show that the two signals often alternate in agreement with the respective A-band and Z-line origin of each signal. 2f sarcomeric SHG-IPs are also observed in the SHG image (arrowheads and arrows in Fig. 2(a)). For TPEF image, 2f sarcomeric TPEF-IPs are also visible in Fig. 2(b) and they are often spatially correlated to 2f sarcomeric SHG-IPs (ROIs indicated by white arrowheads and white filled or empty arrows in Fig. 2(a)-2(c)) as illustrated by intensity profile analysis (Fig. 2(e)). However, we also found regions with 2f sarcomeric SHG-IP spatially correlated to 1f sarcomeric TPEF-IPs (ROIs indicated by yellow filled arrows Fig. 2(a)-2(c)). We found that 60% ($n = 150$ myofibrils from 13 random fields) of 2f sarcomeric SHG-IPs are spatially correlated to 2f sarcomeric TPEF-IPs whereas this percentage is 94% ($n = 32$ myofibrils from 17 random fields) in control muscle. The observed correlation between 2f sarcomeric SHG and TPEF images strongly suggest that these patterns result from the same micro-architectural modification of the muscular tissue.

Spatial correlation between SHG- and TPEF-IPs were also found using a lipophilic fluorescent dye (RS19). This dye is a chemical analog of the voltage sensitive dye Di-6-ASPBS [44] that accumulates in membranes and is used herein to label muscle tubular system, triads and also mitochondria predominantly localized at the I-band [48]. This dye was found brighter with better photo stability compared to alexa-fluor 488 and 594 secondary antibodies often used for TPEF immuno-histological and -cellular imaging therefore enabling good resolution Z-stack imaging. Orthogonal views of both SHG and TPEF-RS19 Z-stack images are illustrated in Fig. 3.

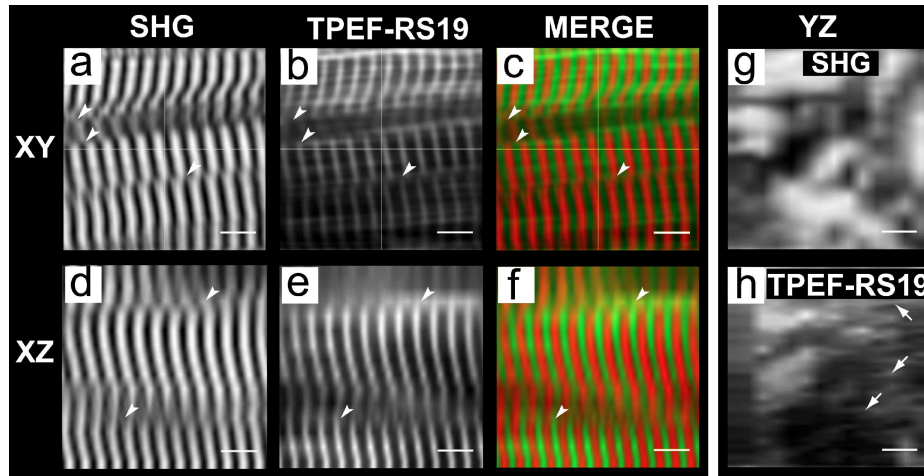


Fig. 3. 3D orthogonal views of SHG and TPEF-RS19 images of mdx mouse gastrocnemius muscle. (a, d), (b, e) and (c, f) are respectively SHG, TPEF and merge of XY and XZ views. Note that for the merge, red and green colors are respectively for SHG and TPEF signals. Note that arrowheads indicate 2f sarcomeric TPEF-IPs spatially correlated to 2f sarcomeric SHG-IPs. (g) and (h) are YZ views of respectively SHG and TPEF images. Arrows indicate resolved tubular system in YZ view of TPEF-RS19 image. Scale bar = 5 μ m.

XY sections of both SHG (Fig. 3(a)) and TPEF (Fig. 3(b)) images showed that the two signals are alternated as expected and illustrated in Fig. 3(c) (merge SHG and TPEF signals). The same alternation of SHG and TPEF signals are also observed in XZ sections (Fig. 3(d)-3(f)) obtained at the center of the Z-stack. A close look at both SHG and TPEF images showed spatially correlated 2f (pitchforklike/Y-shape) IPs (arrowheads). From z-stack images, we found that 87% ($n = 170$ myofibrils from 56 random fields) of 2f sarcomeric SHG-IPs are spatially correlated to 2f sarcomeric TPEF-IPs in mdx muscle. In YZ sections, individual A-bands could not be resolved in the SHG channel (Fig. 3(g)) whereas the tubular system (indicated by arrows) are well resolved along the Y-axis for the TPEF channel (Fig. 3(h)).

Since we have previously shown that angular emission of SHG light is a very sensitive technique to probe myofibrillar displacement below the optical resolution [45], we undertook next SHG-AIP experiments in order to determine the myofibrillar arrangement underlying the spatially correlated 2f sarcomeric SHG- and TPEF-IPs. Experimental SHG images and SHG-AIPs of mdx muscles are shown in Fig. 4. Width of ROI is chosen to be of the order of the size of a sarcomere in order to obtain an average sarcomeric SHG-AIP. SHG-AIP were found to be either two spots (ROIs (1-7)) or one centered spot (ROIs (8-14)) corresponding respectively to well registered and misregistered myofibrillar A-bands [45]. A good correlation was found between 1/ two spots SHG-AIP and 1f sarcomeric SHG-IP and 2/ one spot SHG-AIP and 2f sarcomeric SHG-IP. In the latter case, SHG-AIP with one centered spot was found to be $92\% \pm 3\%$ (177 ROIs from 30 random fields) correlated to 2f sarcomeric SHG-IP, indicating that most 2f sarcomeric SHG-IP is the result of myofibrillar displacement [45].

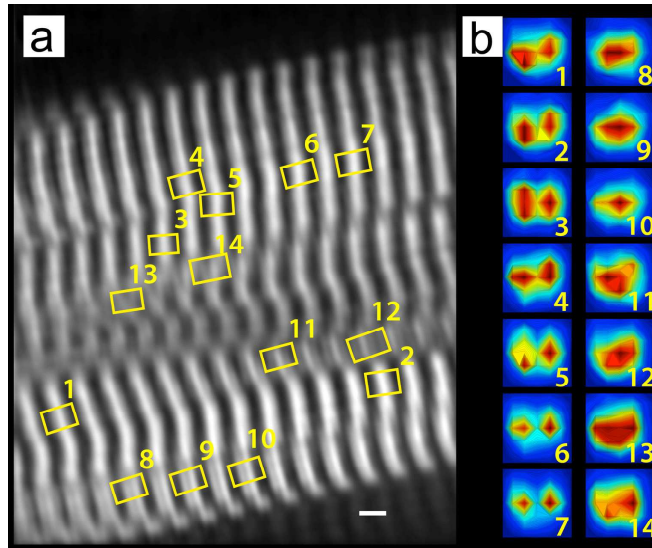


Fig. 4. Experimental SHG image and SHG-AIPs of mdx mouse gastrocnemius muscle. (a) Typical SHG image. (b) SHG-AIP of corresponding ROIs shown in (a). Note that each thumbnail in (b) is labeled by a number localizing the ROI in (a). Full angular width of SHG-AIP for each thumbnail in (b) is 66° in both horizontal and vertical directions. Each SHG-AIP is obtained for 7×7 positions of the pinhole with angular width of 10° . Scale bar = $3 \mu\text{m}$.

As the percentage of 2f sarcomeric SHG-IP is about $20\% \pm 2\%$ ($n = 107$ fields) in random fields of mdx muscle (Fig. 5(a)), spatial correlation between 2f sarcomeric SHG-IP and myofibrillar displacement at TEM level is not straightforward. Fortunately, we consistently found that the percentage of 2f sarcomeric SHG-IP was drastically increased in ROIs of preserved myofibers that were within $20 \mu\text{m}$ of the border of necrotic fibers (Fig. 5(a)). Proximal (within $20 \mu\text{m}$) and distal (between 20 and $50 \mu\text{m}$) regions of preserved fiber bordered by necrotic ones yielded percentage of 2f sarcomeric SHG-IP of respectively $77\% \pm 7\%$ ($n = 18$ fields) and $33\% \pm 5\%$ ($n = 25$ fields) respectively. That clearly indicates a gradient of 2f sarcomeric SHG-IP inside the same myofibers starting in the vicinity of necrotic fibers. Results of TEM studies are illustrated in Fig. 5(b)-5(e). Typical TEM image from control muscle presents tightly closed myofibrils registered at Z-lines (Fig. 5(b)). At higher magnification, thick filaments of A-bands were found centered and well aligned (Fig. 5(c)). Mitochondria are often observed between sarcomeres near Z-lines and triads (structure of T-tubules and terminal cisternae of sarcoplasmic reticulum) are seen close to the I-A-band junction. For mdx muscle images, care was taken to select TEM images encompassing regions of preserved myofibers bordered by necrotic ones as illustrated in Fig. 5(d).

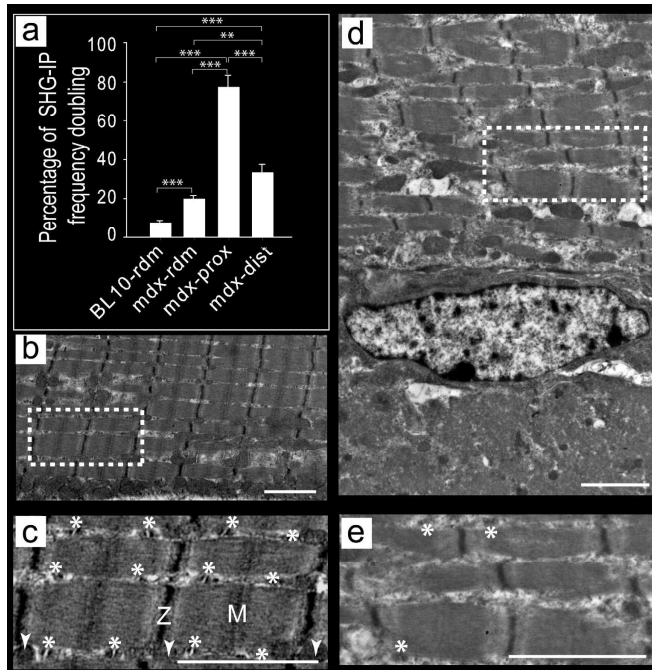


Fig. 5. (a) Histogram representing mean percentage of 2f sarcomeric SHG-IP in random fields of control BL10 fibers (BL10-rdm), random fields of preserved mdx fibers (mdx-rdm), near regions of necrosis inside preserved mdx fibers (mdx-prox) and distal regions of necrosis inside mdx preserved fibers (mdx-dist). Note that asterisk indicates p-value of statistical student t-test (***) $p < 0.001$, ** $p < 0.01$, number of fields n is $70 < n < 100$) (b) Representative EM image of control healthy BL10 gastrocnemius muscle. (c) Enlarge view of ROI indicated in (b) showing tightly joined myofibrils and well-aligned sarcomeres. Z-line and M-band are indicated. Arrowheads and asterisks indicate respectively mitochondria and triads. (d) Representative TEM image of mdx muscle tissue. Adjacent sarcomeres misaligned by half a sarcomere size are indicated by arrowheads. Note the absence of sarcomeric striation of a necrotic fiber at the bottom of the preserved fiber. (e) Magnified TEM image of ROI indicated in (d) showing 6 typical sarcomeres of 3 myofibrils. Note that myofibrils are misaligned and that triads are barely visible. Scale bar = 2 μm .

As expected myofibrils disorganization with Z-lines and A-bands misalignment are observed. Quantitative measurement of the distance separating sarcomeric A-bands between adjacent myofibrils were obtained in proximal regions ($\leq 20 \mu\text{m}$) of necrotic fibers. These values were found to be $237 \pm 257 \text{ nm}$ ($n = 154$ A-bands) in proximal regions in mdx muscles which is significantly greater ($p < 0.001$) than $20 \pm 48 \text{ nm}$ ($n = 403$ A-bands) found in control. At higher magnification (Fig. 5(e)), we notice that thick filaments inside A-band were often centered. Moreover, number of triads was found to be drastically reduced. Quantitative measurement of the average number of triads bordering a sarcomere was found to be 3.1 ± 0.1 ($n = 119$ triads) in control and this value was reduced ($p < 0.001$) to 1.4 ± 0.1 ($n = 119$ triads) in mdx muscles. In addition to Z-lines misregistration, myofibrillar disruption was occasionally observed (Fig. 5(d),5(e)) indicating proteolysis of both cytoskeleton and sarcomeric proteins as expected [12]. TEM results indicate that 2f sarcomeric SHG-IPs result from A-bands misregistrations that are spatially correlated to triad disruptions.

4. Theoretical simulation of SHG- and TPEF-IPs

In order to clearly correlate A-bands misregistrations observed at TEM level and 2f sarcomeric SHG-IPs of preserved gastrocnemius mdx fibers, we undertook theoretical simulation of SHG-IPs. Characteristic results of the theoretical simulation for misaligned myofibrils along myofibrillar axis (x direction) are illustrated in Fig. 6.

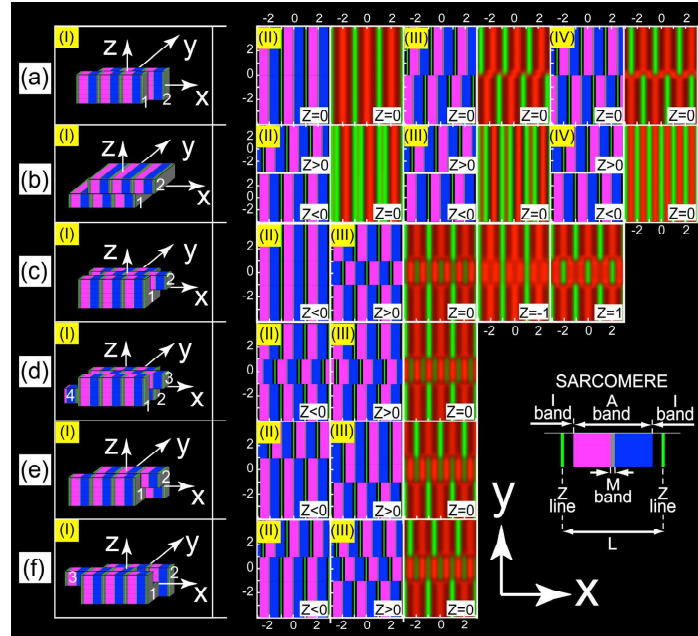


Fig. 6. Macroscopic and microscopic diagrams illustrating different myofibrillar organization and their corresponding theoretical SHG (myosin, red color) and TPEF (immunodetection of Z-line α -actinin, green color) intensity patterns for a sarcomere size of $L = 2 \mu\text{m}$. For all simulations, overall thickness of the myofibrillar bundle is $z = 6 \mu\text{m}$ and laser beam that is propagating along z direction, is focused at $z = 0$ at the middle of the bundle. For the calculation, each bundle was decomposed in individual myofibrils of rectangular size $1 \mu\text{m} \times 1 \mu\text{m}$ in y and z directions (see theoretical simulation). For all microscopic schematic views, A-bands consist of well-ordered thick filaments that are represented by a double color code (magenta and blue) to account for polarity inversion at the M-band (grey color) and immunodetection of Z-line α -actinin is shown in green color. A schematic view of the sarcomere is shown in inset (lower right corner). (a) Macroscopic schematic diagram of two bundles with parallel XZ planes misaligned in x direction at $y = 0$. Microscopic schematic diagrams (left) and their corresponding theoretical SHG and TPEF intensity patterns (right) of aligned (aII), misaligned by $L/4$ (aIII) and misaligned by $L/2$ (aIV) A-bands. Note that for misalignment of $L/2$ SHG-IP has a Y-shape. Note also that in addition to the intra sarcomeric A-band polarity inversion (in x direction), inter A-band polarity inversion (in y direction) between adjacent myofibrils occurs at $y = 0$ due to myofibrillar misalignment. (b) Macroscopic schematic diagram of two bundles with parallel XY planes misaligned in x direction at $z = 0$. Microscopic schematic diagrams (left) and their corresponding theoretical SHG and TPEF intensity patterns (right) of misaligned A-bands. Values of misalignment are $L/4$ (bII), $L/3$ (bIII) and $L/2$ (bIV). (c) Macroscopic schematic diagram representing two bundles with respectively U-shape (1) and rectangular shape (2) misaligned by $L/2$ at $z = 0$. Microscopic schematic diagrams at $z < 0$ (cII) and $z > 0$ (cIII) and the corresponding theoretical SHG and TPEF intensity patterns at $z = 0$, $z = -1$ and $z = 1$ as indicated. Note that misalignment induces appearance of additional polarity inversion of adjacent hemi A-bands along z direction at $y = 0$. Note that for all three z positions, SHG-IPs have rectangular-shape. (d) Macroscopic schematic diagram representing four bundles with rectangular shape. Bundles 1 and 2 are well aligned and bundles 3 and 4 are misaligned from bundles 1 and 2 by $L/4$ and in opposite direction. Microscopic schematic diagram at $z < 0$ (dII) and $z > 0$ (dIII) and the corresponding theoretical SHG and TPEF intensity patterns at $z = 0$ as indicated. Note the $L/4$ shift of $2f$ sarcomeric SHG- and TPEF-IPs when compared to (c). Note that SHG-IP has a vernier-shape. (e) Macroscopic schematic diagram of two L-shape bundles misaligned by $L/2$. Microscopic schematic diagram at $z < 0$ (eII) and $z > 0$ (eIII) and the corresponding theoretical SHG and TPEF intensity patterns at $z = 0$ as indicated. Note that SHG-IP has a staircase-shape. (f) Macroscopic schematic diagram of three misaligned bundles with respectively L-shape (1) and rectangular shape (2, 3). Bundles 1, 2 and 1, 3 are misaligned by respectively $L/4$ and $L/2$. Microscopic schematic diagram at $z < 0$ (fII) and $z > 0$ (fIII) and the corresponding theoretical SHG and TPEF intensity patterns at $z = 0$ as indicated. Note that SHG-IP has a U-shape. Scales of the microscopic diagrams and of the theoretical simulations are in μm .

All simulations are obtained using the experimentally measured sarcomere size of $L = 2 \mu\text{m}$. The first panel of each row is a schematic macroscopic 3D view of a portion of muscle tissue representing a particular case of myofibrillar displacement. The other panels of each row are microscopic views of either xy schematic diagrams of myofibrillar organization or their corresponding theoretical SHG- (red color) and α -actinin (green color) TPEF-IPs. For all microscopic schematic views, A-bands (size $1.6 \mu\text{m}$) consist of well-ordered thick filaments that are represented by a double color code (magenta and blue) to account for polarity inversion at the M-band (grey color) due to antiparallel polymerization of myosin molecules. α -actinin marker of the Z-line is shown in green color. I-bands are in dark color and thin band with grey color at the center of each A-band corresponds to the M-band region (size $m = 150 \text{ nm}$) with antiparallel overlapping of myosin thick filaments where no SHG signal is produced (see the schematic view of the sarcomere in inset of Fig. 6). All segments of myofibrils are shown with a series of 3 sarcomeres. Figure 6(a), 6(b) illustrates cases of two bundles of myofibrils characterized by respectively parallel XZ and XY planes that are misaligned along x direction. Simulation shows that misalignment induces 2f sarcomeric SHG-IPs at $y = 0$ (Fig. 6(a)) and at $z = 0$ (Fig. 6(b)). Theoretical simulations of Fig. 6(a), 6(b) correspond to experimental results of Fig. 2 indicated respectively by empty arrowheads and filled white arrows. Moreover, Y-shape SHG-IPs are observed for misaligned XZ planes but not for XY planes. Therefore, shape of 2f sarcomeric SHG-IPs can provide information about the orientation of the shear planes as further illustrated in Fig. 6(c)-6(d). Altogether, these theoretical results show that the result of a myofibrillar displacement along myofibrillar main axis is the appearance of 2f sarcomeric SHG-IP.

4. Discussion

The major finding of this study is that preserved myofibers of mdx muscle tissue are characterized by an increase of 2f sarcomeric SHG- and TPEF-IPs correlated to myofibrillar displacement as suggested by SHG-AIP and also observed at ultrastructural TEM level. Moreover, ultrastructural studies revealed a good spatial correlation between myofibrillar misalignment and triad disappearance. Theoretical simulation also demonstrates that myofibrillar misalignment always results in the appearance of 2f sarcomeric SHG-IP due to constructive interferences of harmonic photons emitted from misaligned adjacent hemi A-bands of inverse polarity [42, 45]. Y- or vernier-shape SHG-IPs have been previously reported in mdx muscle as the result of either myofibrillar deformation or change of myosin orientation between different arms of the Y- or vernier-shape [20]. Our results show that Y-shape SHG-IP is an optical illusion due to myofibrillar misalignment and should not be confused with myofibrillar deformation. This Y-shape optical illusion originates from over intensities appearing both at the M-band (stem) and between neighboring A-bands of adjacent myofibrils (arms) as a result of constructive interferences of harmonic photons emitted within the PSF [42]. A major finding from theoretical simulation is that Y-shape SHG-IP is the result of myofibrillar misalignment of the order of $L/2$. However, mean myofibrillar displacement found at TEM level is $237 \pm 257 \text{ nm}$, a value lower than the one found at optical level and which could be explained by sample shrinkage due to its deshydration prior TEM imaging [49].

From theoretical analysis, we also suggest that combined SHG-IP and SHG-AIP experiments should be sufficient to determine the level of (inter- or intra-sarcomeric) myosin thick filaments disorganization as illustrated in Fig. 7. Well-registered A-bands of relax healthy muscles are characterized by 1f sarcomeric SHG-IP and two-distant-spots SHG-AIP (Fig. 7(a)). Misaligned myofibrils of proteolysed or disease muscles are characterized by combined 2f sarcomeric SHG-IP and two-closed-spots SHG-AIP (Fig. 7(b)). According to the experimental angular resolution, these closed spots become one-centered spot as shown in the second column of Fig. 4(b). Fine analysis of the contrast of 2f sarcomeric SHG-IPs is sufficient to discriminate between intra-sarcomeric myosin thick filaments disorder [46] (Fig.

7(c)) and mini sarcomeres (Fig. 7(d)) previously described during developmental myofibrillogenesis [50, 51]. Therefore, combining both SHG-IP and SHG-AIP enables to probe the 3D arrangement of myosin thick filaments in the focusing volume. Since it takes less than ten minutes to acquire both SHG-IP and SHG-AIP images, these techniques are compatible with live imaging of muscle tissue. As they are sensitive to the phase of the emitted harmonic waves and therefore to the spatial modulation of density and polarity of the nonlinear emitters within the focusing volume, they probe myofibrillar displacement below the optical resolution [42, 45]. For example backward SHG signal probes spatial modulation of nonlinear emitters at the scale of about $\lambda/10$. However they do not directly measure the phase of nonlinear emitters as can be done by interferometric SHG microscopy [52, 53]. The drawback of this latter technique is the acquisition time which is of the order of a few hours to fully characterize a scanned area [53]. Therefore improving the acquisition time to reduce phototoxicity and mechanical drift might be necessary for this latter technique to be fully compatible with live imaging. All together these phase sensitive techniques probe spatial modulation of the supramolecular nonlinear optical susceptibility $\chi^{(2)}$ whereas polarization microscopy provides information on the orientation of the molecular hyperpolarizability $\beta^{(2)}$. Polarization microscopy has been shown to provide dynamic conformation change of thick filaments cross bridge occurring during isometric contraction [37]. However, the main limitation of this technique is that it is too slow to follow a twitch contraction.

We have previously reported 2f sarcomeric SHG-IP in experimentally induced proteolysed muscle in xenopus, rat and in pathological mdx mouse. This report brings new information concerning myofibrillar misalignment correlated to triad disappearance of pathological mouse muscle probed by SHG, TPEF and TEM. More precisely the novelty of our results can be summarized as follow. 1/ We show quantitatively (by measuring the percentage of 2f sarcomeric IPs) that SHG is more sensitive than TPEF to probe myofibrillar misalignment. Indeed, due to its coherent nature, emitted SHG signal is sensitive to the phase of the harmonic waves enabling to probe the relative organization of nonlinear SHG emitters within the focusing volume. 2/ Quantification of 2f sarcomeric SHG-IPs shows that they are predominantly clustered near necrotic fibers. Since myo-necrosis regions are localized and clustered in small areas (representing less than 10% of the whole muscle tissue in 6 weeks mdx muscles (see also [47]), percentage of 2f sarcomeric SHG-IPs in proximal and distal regions of necrosis were always greater than the one found in random areas (Fig. 5(a)). 3/ Necrotic regions were used as structural markers to correlate 2f sarcomeric SHG-IPs to myofibrillar misalignment and to triad reduction. The latter result is expected to have important functional consequence by impairing EC coupling. 4/ Theoretical simulation (Fig. 6) has been used to explain the variety (Y-shape, vernier-shape, U-shape etc.) of 2f sarcomeric SHG-IP observed (Fig. 2) and related to 3D myofibrillar misalignment. Moreover, simulation of combined 2D images of SHG-IP and TPEF-IP has never been presented before. This approach enables 3D micro architectural mapping of sarcomeres in muscle tissue. Furthermore, theoretical simulation put forward that intra-sarcomeric thick filament disorder, mini sarcomeres and myofibrillar misalignment resulting in 2f sarcomeric SHG-IP can all be discriminated by combining both SHG-IP and SHG-AIP.

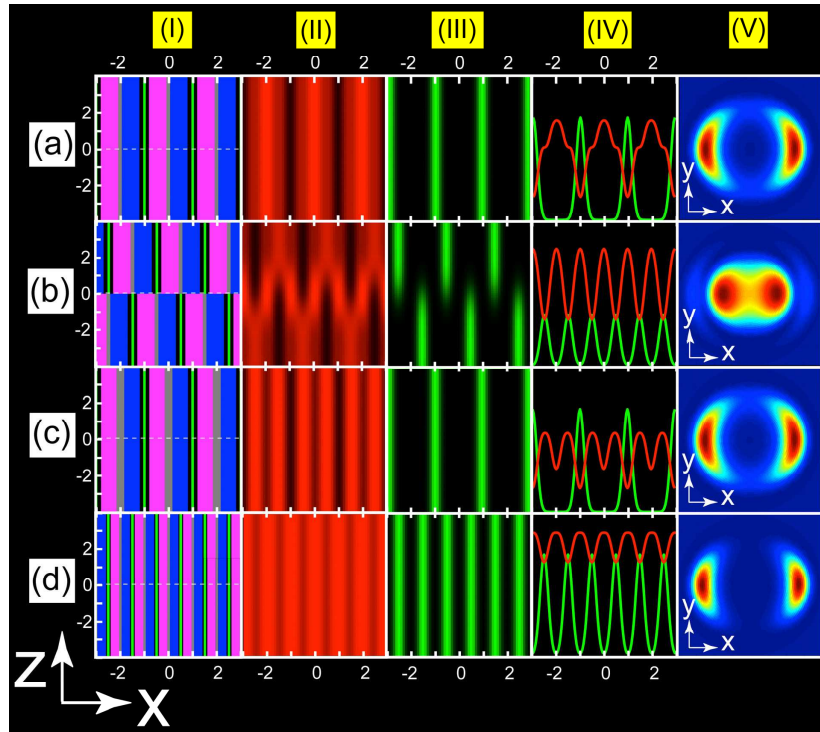


Fig. 7. Theoretical simulation of SHG and TPEF signals of different cases of myofibrillar arrangement. (a-d) are respectively well registered A-bands (a), misaligned A-bands by $L/2$ (b), well registered A-bands with misaligned thick filaments (c) and mini sarcomeres (d). (a,b) $L = 2 \mu\text{m}$, $A = 1.6 \mu\text{m}$ and $m = 150 \text{ nm}$. (c) $L = 2 \mu\text{m}$, $A = 1.6 \mu\text{m}$, $m = 320 \text{ nm}$. (d) $L = 1 \mu\text{m}$, $A = 0.8 \mu\text{m}$, $m = 150 \text{ nm}$. (I-V) are respectively schematic diagrams, SHG-IPs, TPEF-IPs, Intensity profiles at $z = 0$ and SHG-AIPs. Note that (I-IV) are XZ views whereas (V) is a XY view. Color codes for (I-III) are identical to those of Fig. 6 and color code of (IV) is red and green for respectively SHG and TPEF intensity profiles. For (V), SHG-AIPs are in arbitrary units with increasing intensity from *blue* to *red*. Full angular widths of SHG-AIPs are 66° in both x and y directions. Note the scale in μm for I-IV.

It has been suggested that mdx mouse are characterized by an increase in fraction of hyper contracted sarcomeres corresponding to decrease in mean sarcomere length due to impaired calcium homeostasis [30]. In agreement with this study, we found high frequency ($2f$) sarcomeric SHG-IP. However, in our experimental conditions, we did not find any hyper contracted sarcomeres with both SHG and TEM images. In the absence of TEM images in this previous study [30], one could not exclude that the presumed hyper contraction is either experimentally induced or a misinterpretation of high frequency SHG-IP. Increase in $2f$ sarcomeric SHG-IPs that we observed in mdx muscle is in agreement with previous report [20] and could be the consequence of oxidative stress as experimentally shown in non-disease muscles [40, 41]. Loss of transverse myofibrillar alignment described herein in mdx muscle using both SHG and TPEF imaging has been previously reported in human dystrophic and DMD muscles [12]. In this latter report, sarcomeric misalignment has been explained at TEM level as resulting from excessive antagonist forces generated by hyper contraction and stretching of the muscle at different locations leading to the breakdown of the intermediate filament protein desmin that connect adjacent sarcomeric Z-lines. In agreement with this ultrastructural study, myofibrillar impairment present in all mdx muscle fibers has been suggested to underlie the enhanced force loss observed after eccentric contractions [8]. In addition to the correlation between $2f$ sarcomeric SHG-IP and A-band misalignment, we found a second correlation between $2f$ sarcomeric SHG-IP and triad reduction. Whether the

latter is a consequence of the former or vice versa is not known. For the former correlation, the mechanism of myofibrillar displacement inducing 2f sarcomeric SHG-IP has been recently reported in details for xenopus gastrocnemius muscle [42]. The second correlation suggests that 2f sarcomeric SHG-IP could be used to probe excitation contraction coupling alteration. In mdx muscle, mechanical stress has been shown to induce calcium release [10, 18, 54], activation of calcium-dependent proteolysis [55] and alteration of the excitation contraction coupling [8, 15–17]. Future functional and spatial study combining SHG microscopy, calcium fluorescence and force measurement will provide sub-micrometric spatial resolution and complementary information to electrophysiological studies that integrate the electric signal at a higher level corresponding to the whole myofiber. Disruption of the excitation contraction coupling has been reported in several other striated muscle disease including heart [56–60] and muscle damage induced by eccentric contractions [8]. Structural myofibrillar disorganization has also been observed in several animal and human skeletal muscle gene diseases [12, 48, 61–63]. However information regarding the structural involved mechanism, their spatial localization and distribution at sub-micrometric scale is scarce or lacking. SHG microscopy opens new avenues for functional studies aimed at filling this gap.

5. Conclusion

The main finding of this study is that increase of frequency doubling sarcomeric SHG intensity pattern observed on mdx mouse gastrocnemius muscle is the result of myofibrillar displacement observed at TEM level and demonstrated by theoretical simulation. More importantly, these myofibrillar displacements were correlated with triad disruption. Based on theoretical simulation of sarcomeric SHG intensity pattern, we show that SHG microscopy emerges as a powerful tool to reveal the submicrometric organization of A-band thick filaments. We anticipate that SHG microscopy will be of paramount to gain insight in triad defects and excitation contraction disruption that occurs during muscle physiological adaptation and disease.

Acknowledgments

This work was supported by Région Bretagne, Rennes Métropole, Conseil Général d'Ille-et-Villaine, CRITT Santé Bretagne, Ministère de l'Enseignement Supérieur et de la Recherche and the European Union Federal Funds FEDER.